

Anti-Oxygen Leaking LiCoO₂

Soroosh Sharifi-Asl, Fernando A. Soto, Tara Foroozan, Mohammad Asadi, Yifei Yuan, Ramasubramonian Deivanayagam, Ramin Rojaee, Boao Song, Xuanxuan Bi, Khalil Amine, Jun Lu, Amin Salehi-khojin, Perla B. Balbuena,* and Reza Shahbazian-Yassar*

LiCoO₂ is a prime example of widely used cathodes that suffer from the structural/thermal instability issues that lead to the release of their lattice oxygen under nonequilibrium conditions and safety concerns in Li-ion batteries. Here, it is shown that an atomically thin layer of reduced graphene oxide can suppress oxygen release from Li_xCoO₂ particles and improve their structural stability. Electrochemical cycling, differential electrochemical mass spectroscopy, differential scanning calorimetry, and in situ heating transmission electron microscopy are performed to characterize the effectiveness of the graphene-coating on the abusive tolerance of Li_xCoO₂. Electrochemical cycling mass spectroscopy results suggest that oxygen release is hindered at high cutoff voltage cycling when the cathode is coated with reduced graphene oxide. Thermal analysis, in situ heating transmission electron microscopy, and electron energy loss spectroscopy results show that the reduction of Co species from the graphene-coated samples is delayed when compared with bare cathodes. Finally, density functional theory and ab initio molecular dynamics calculations show that the rGO layers could suppress O₂ formation more effectively due to the strong C–O_{cathode} bond formation at the interface of rGO/LCO where low coordination oxygens exist. This investigation uncovers a reliable approach for hindering the oxygen release reaction and improving the thermal stability of battery cathodes.

1. Introduction

From the early adoption of Li-ion battery systems in portable electronics, thermal runaway incidents have always been a

major concern.^[1,2] However, despite the great progress in improving the electrochemical properties of Li-ion batteries, their safety aspects have not advanced significantly, as many still confront thermal runaway incidents in the Li-ion battery containing devices.^[3,4] Integration of the Li-ion batteries into the electric vehicle and large-scale transportation systems further stresses the importance of the Li-ion battery thermal stability and safety issues.^[5–7] Thus, efforts are underway to better understand the thermal runaway events. In general, thermal runaway is the outcome of a chain of reactions that take root from a slight temperature rise caused by overcharge, fast cycling or high ambient temperature.^[8,9] Under these circumstances, cell temperature rises and causes the decomposition of the organic electrolyte, releasing flammable gases. Subsequently, oxide-based cathodes such as LiCoO₂ will decompose and lose their lattice oxygen. The released oxygen can ignite the flammable gases, which are heated beyond their flash point, leading to the thermal runaway.^[10–12]


Considering the importance of the layered oxide cathode materials in the commercialization of the lithium-ion batteries, various experimental studies using in situ X-ray diffraction/absorption spectroscopy,^[13–17] thermal analysis,^[18–23] in situ transmission electron microscopy (TEM)^[24–26] and computational efforts^[27,28] were carried out to characterize and understand the oxygen-release phenomenon and the thermal degradation mechanisms in these materials. Overall, it is understood that the extraction of Li-ions from the cathode unit cell results in the formation of under-coordinated oxygen atoms, which destabilizes the structure.^[28] At elevated temperatures these under-coordinated oxygens break the bonds with the transition metals and form O₂ molecules leaving the host structure. As a result, the layered structure will rearrange to form the spinel and the rocksalt phases that contain less oxygen in their unit cell.^[26] It has been shown that the extent of oxygen release is dependent on the surface fraction of the particles.^[18]

In addition to safety aspects, there has been a strong thrust in improving the cycling stability and Li-intercalation kinetics of LiCoO₂. In this context, synthesis of high surface area structures such as nanorod arrays^[29] or porous nanosheet 3D structures^[29] of LiCoO₂ have been carried out to achieve fast

S. Sharifi-Asl, T. Foroozan, Dr. M. Asadi, Dr. Y. Yuan, R. Deivanayagam, R. Rojaee, B. Song, Prof. A. Salehi-khojin, Prof. R. Shahbazian-Yassar
Mechanical and Industrial Engineering Department
University of Illinois at Chicago
Chicago, IL 60607, USA
E-mail: rsyassar@uic.edu

Dr. F. A. Soto, Prof. P. B. Balbuena
Department of Chemical Engineering
Texas A&M University
College Station, TX 77843, USA
E-mail: balbuena@tamu.edu

Dr. Y. Yuan, Dr. X. Bi, Dr. K. Amine, Dr. J. Lu
Chemical Science and Engineering Division
Argonne National Laboratory
9700 S. Cass Avenue, Argonne, IL 60439, USA

 The ORCID identification number(s) for the author(s) of this article can be found under <https://doi.org/10.1002/adfm.201901110>.

DOI: 10.1002/adfm.201901110

intercalation kinetics and flexible Li-ion batteries. However, since many degradation mechanisms including the parasitic oxygen release reaction, are surface and subsurface originated,^[30–33] various approaches such as coating,^[34–39] surface passivation,^[40,41] synthesis of core-shell structures^[42–44] and chemical gradient compositions^[45] have been pursued for improving the cyclability and stability of cathode materials. For instance, it has been shown that coating the LiCoO₂ cathodes with Al, F-based material that forms a Li-Co-Al-F-O solid solution beneath the surface can improve the structural stability of LCO when operating at 4.6 V. Similarly, AlPO₄ coating on LiCoO₂ has shown to effectively prevent the oxygen release reaction and inhibit the over-charge induced thermal runaway reaction.^[13] However, large thickness of surface coatings that can potentially increase the charge transfer resistance, the presence of porosities that can allow for O₂ release, decomposition and instability of the coating material,^[46] uniformity issue associated with deposition techniques and high cost of deposition methods, slow down the inclusion of this approaches into the industry.

In order to improve the thermal stability of the cathodes and simultaneously maintain the electrochemical properties, the surface coating of cathodes should meet a number of requirements: 1) it should be impermeable to the oxygen gas but allow for the Li-ion transfer, 2) have high electronic conductivity, 3) remain stable in contact with the electrolyte, and 4) be scalable and cost effective.^[47] In this regard, atomically thin graphene and its derivatives such as reduced graphene oxide (rGO) appear to be good candidates since it has been shown that graphene and rGO are impermeable to liquids^[48,49] and gases specially oxygen.^[50–55] Reduced graphene-oxide has shown a great potential in the gas barrier applications.^[56] Also, the rGO membranes are leak-tight against various gasses such as He, N₂, and O₂^[57] since the transfer of gas molecules through the rGO layers cannot happen in out-of-plane direction and can only occur through the gaps between the individual rGO sheets and through the interlayer spacings. Therefore, by reduction of GO to rGO and reduction of interlayer distance from 10 to 4 Å, the diffusivity of molecules can be effectively decreased.^[58] In another study, the layer by layer deposition of few layer rGO through electrostatic bond formation (similar to our case) is shown to decrease the oxygen transfer rate (OTR) of poly(ethylene terephthalate) substrates by 95%.^[59] In another work, rGO/polyimide films prepared by in situ polymerization showed to decrease the OTR by 93% compared to pure PI films.^[60] Therefore, our goal was set to utilize the gas barrier properties of rGO to inhibit the release of O₂ in the thermal decomposition reaction of LiCoO₂. A conformal thin coating of rGO that does not compromise the ionic transport was achieved and O₂ release phenomenon was characterized under high-voltage and high-temperature conditions. Reduced graphene oxide also benefits from a number of other properties such as superior electronic and ionic conductivity,^[61–63] high mechanical flexibility^[64] and stability in long electrochemical cycling.^[65] Herein, we demonstrate coating of individual LiCoO₂ cathode particles with reduced graphene oxide to suppress the oxygen release from the layered oxide cathodes under high-temperature and harsh electrochemical cycling. Using a broad range of electrochemical measurements and materials characterization

techniques, such as high voltage cycling, DEMS measurements, in situ heating TEM and thermal analysis, we demonstrated that rGO-coating can successfully mitigate the oxygen release and improve the structural stability of LiCoO₂.

2. Results and Discussion

Figure 1A is a schematic representation of the coating procedure. The surface charge of the LiCoO₂ particles is modified to facilitate the self-assembly of negatively charged GO nanosheets with positively charged LiCoO₂ particles. Subsequently, GO is reduced to rGO through the hydrazine treatment^[66] to improve the electrical conductivity and allow for the Li-ion transport. Figure 1B shows the SEM images from several individual LiCoO₂ particles coated with graphene layers. Figure 1C presents high-magnification SEM images from the indicated areas to better illustrate the graphene-coating of individual LiCoO₂ particles. The presence of the ultra-thin graphene can be identified from the graphene wrinkles at the surface of the particles. Further characterization of the graphene-coating LiCoO₂ sample was carried out utilizing high-resolution transmission electron microscopy (HR-TEM), electron diffraction analysis, Raman and XPS spectroscopy. From the HRTEM image shown in Figure 2A, a ≈ 2 nm layer of rGO consist of 3–5 layers can be seen on the surface of the LiCoO₂ particle. Additional TEM images to confirm the uniformity of coating thickness are demonstrated in Figure S1 (Supporting Information). Intensity profile (inset) from the rGO coating illustrates the presence of four rGO layers, each ≈ 0.41 nm thick. It should be noted that thickness of the mono layer GO and rGO is reported to be 1.1 ± 0.1 and 0.5 ± 0.2 nm respectively.^[67,68] Therefore, it can be concluded that reduction of initial GO layers is achieved by the hydrazine treatment. Also, electron diffraction pattern (shown at the bottom right inset) suggests that the original layered ($R\bar{3}m$) structure of LiCoO₂ is maintained after the graphene-coating process. Figure 2B, presents the Raman results from the bare and the graphene-coating sample and illustrates the presence of reduced graphene oxide peaks without affecting the bonding properties of LiCoO₂ particles. Raman active E_g and A_{1g} modes generated from oxygen vibrations in $R\bar{3}m$ LiCoO₂ can be observed at 482 and 596 cm⁻¹ respectively.^[69] Reduced graphene oxide D peak and G peak generated from sp² carbon lattice can be observed at 1345 and 1595 cm⁻¹ respectively with (I_D/I_G) = 1.71.^[61] X-ray photoelectron spectroscopy (XPS) is also performed on graphene-coated LiCoO₂ samples to confirm the reduction of GO layers to rGO through the hydrazine treatment. As can be seen from Figure 2C, the proportion of oxide groups in the C1s peak is small and shows that GO is successfully reduced to rGO.

The electrochemical performance of the graphene-coated LiCoO₂ under high-voltage cycling condition (voltage window of 3.3–4.8 V at 0.5 C rate) was evaluated and compared with the bare sample. Figure 2D,E show the first four charge/discharge curves of the samples. Both samples show the first charge capacity of about 250 mAhg⁻¹ that is typically observed in LiCoO₂ samples.^[70] The hexagonal to monoclinic phase transition in the capacity range of ≈ 135 mAhg⁻¹ is evidenced by the change of the plateaus at 4.2 V in both samples. Also,

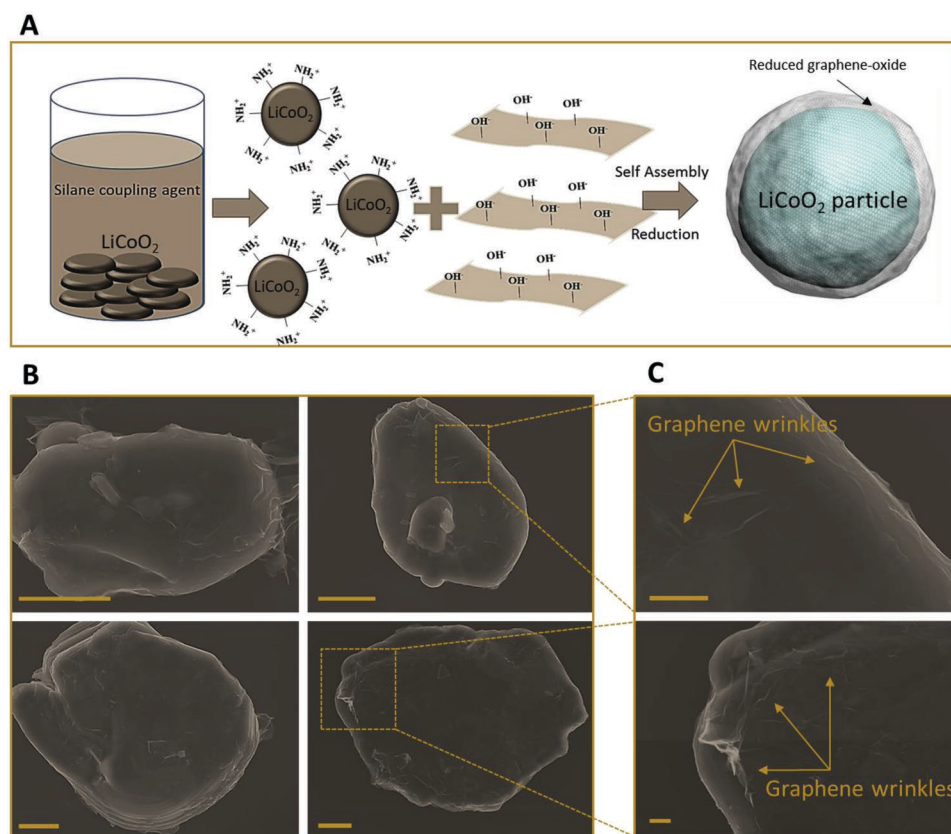


Figure 1. Illustration of graphene-coating method and the confirmation of graphene coverage on the surface of cathode particles. A) Schematic illustration of the coating process. The surface of LiCoO₂ particles is charged positively to facilitate the self-assembly with negatively charged graphene oxide nanoflakes. The resulting material will be individual graphene-coated LiCoO₂ particles. B) SEM images from several individual LiCoO₂ particles after graphene-coating (scale bars are 2 μm). C) High-magnification SEM images from the areas indicated in panel (B). Graphene wrinkles can be clearly observed on the surface of LiCoO₂ particles (scale bars are 500 nm).

two plateaus corresponding to the formation of H1-3 and O1 phases can be clearly observed at >4.5 V in the curve of bare LiCoO₂. O1 is the hexagonal form of rhombohedral O₃ Li_xCoO₂ and H1-3 is considered as the transition structure with a hybrid rhombohedral/hexagonal phase.^[71,72] The origin of these phase transformations are suggested to be the glide of partial dislocations formed as a result of excessive extraction of Li ions, which eventually provide a path for cation mixing and formation of spinel phase.^[73–75] Also, it is suggested that partial reduction and dissolution of Co at the surface of particles due to direct contact of the cathode surface with the electrolyte is another degradation mechanism, which results in capacity loss and failure of the LiCoO₂ cathode.^[76,77] However, the coating of cathode particles will put a barrier in the contact of cathode particles and the electrolyte and possibly hinders the Co dissolution. Nevertheless, the cationic migration leading to partial phase transition that occurs throughout the particles thickness will occur in the graphene-coated sample regardless of the surface condition. Hence, we observed capacity/voltage fade in smaller extents compared to the bare sample. Noteworthy, a higher over-potential in the voltage profile of the graphene-coated sample at the first cycle can be observed. Most probably, this corresponds to the required energy for the Li-ion pathway formation in the coating rGO layers at the first cycle. To confirm

that the graphene-coating is effectively suppressing the oxygen release from the cathode structure, we performed in situ differential electrochemical mass spectrometry (DEMS) experiment on the bare and the graphene-coated LiCoO₂ samples (Figure 2F). DEMS experiment was conducted during the linear sweep voltammetry measurement in the potential window of 3–5.0 V. The results from the cell containing the bare LiCoO₂ cathode shows the evolution of O₂ at ≈4.7 V^[78] while the results from the graphene-coated LiCoO₂ cathode exhibited almost no O₂ evolution throughout the experiment. These results confirm that the graphene-coating completely suppresses the evolution of oxygen during the CV test at high voltages.

Additionally, electrochemical cycling experiments in lower cut-off voltage were performed to evaluate the effect of graphene-coating on the cycling stability of LiCoO₂ cathodes under equilibrium conditions, where the organic electrolytes are stable and various degradation mechanisms that activate as a result of excessive Li-removal from the cathodes (e.g., slab sliding, cationic migration and structural transformation to H1-3 and O1 phases) do not occur.^[73,74,79] As can be seen from Figure 3A, the bare and the graphene-coated LiCoO₂ cathodes have been cycled for 200 cycles in the voltage limit of 3.0–4.2 V with the current rate of C/10 for the initial formation cycle, followed by 1C current rate for the rest of the experiment.

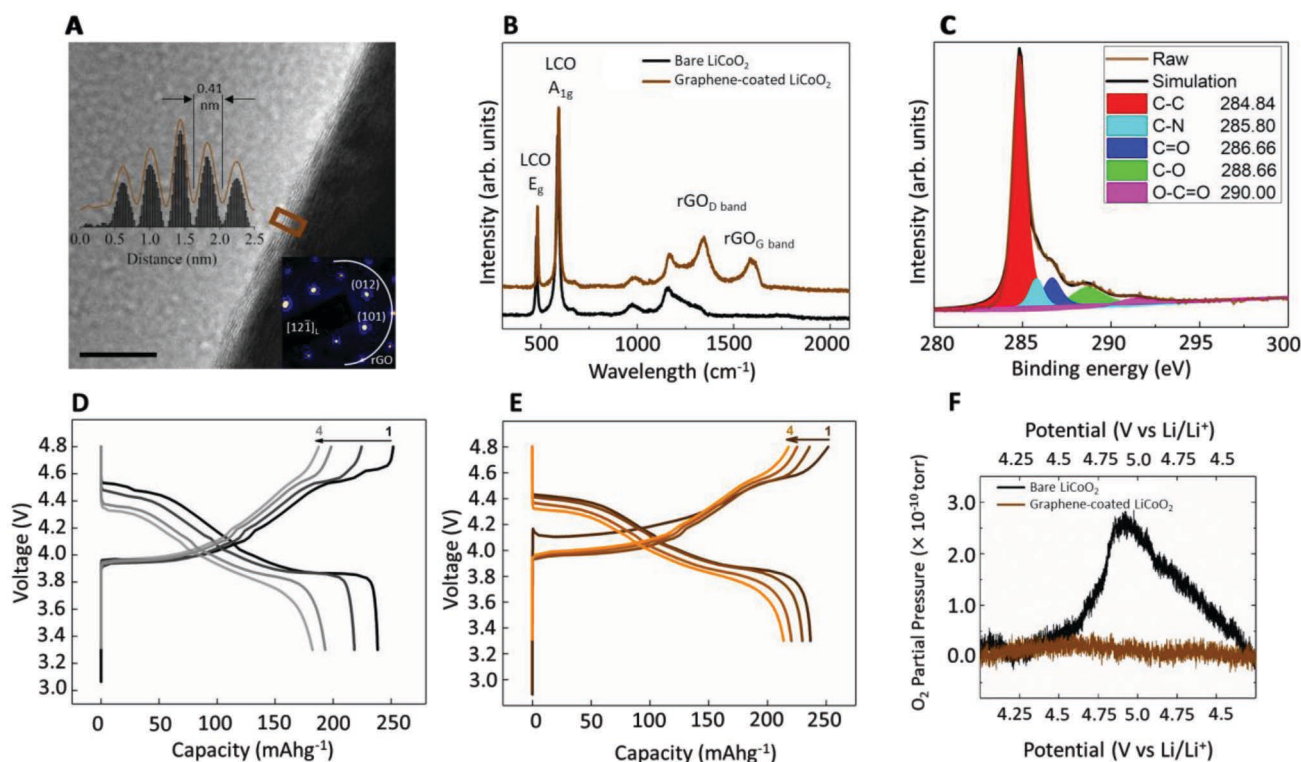


Figure 2. Characterization and high-voltage cycling stability evaluation of graphene-coated LiCoO₂ samples. A) High-resolution TEM image of a graphene-coated LiCoO₂ particle and the corresponding diffraction pattern shown in the inset. Few layers of rGO coating can be observed on the surface of the LiCoO₂ particle. Diffraction pattern shows that LiCoO₂ has retained its original layered structure after the graphene-coating process. The intensity profile is shown in the inset from the red-colored rectangular shows that the rGO coating consists of 3–5 layers of rGO each about 0.41 nm thick and the overall coating thickness is below 2 nm (scale bar is 10 nm). B) Raman spectrum from the bare and the graphene-coated LiCoO₂ sample. Raman active E_g and A_{1g} modes generated from oxygen vibrations in R3̄m LiCoO₂ can be observed at 482 and 596 cm⁻¹ respectively. Reduced graphene oxide D peak and G peak generated from sp² carbon lattice can be observed at 1345 and 1595 cm⁻¹, respectively with (I_D/I_G) = 1.71. C) High-resolution XPS scan from C 1s, minimal fraction of carbon bonding with O and N confirms the reduction of GO coating to rGO. D) Voltage profile of bare LiCoO₂ cycled at 3.3–4.8 V. E) Voltage profile of the graphene-coated LiCoO₂ cycled at 3.3–4.8 V. F) Differential electrochemical mass spectroscopy (DEMS) results from the bare and the graphene-coated LiCoO₂ during cyclic voltammetry (CV) experiment in the potential window of 4–5.2 V versus Li/Li⁺.

Cycling results demonstrate superior capacity retention for the graphene-coated sample. While the capacity retention of the bare LiCoO₂ is ≈55% after 200 cycles,^[80] the graphene-coated sample has retained about 85.9% of its initial capacity. This enhancement can be attributed to the prevention of direct contact between the electrolyte and the cathode surface, which protects the cathodes against detrimental interface reactions such as HF attack and Co dissolution.^[81–84] Furthermore, the electrochemical impedance spectroscopy (EIS) analysis was performed to evaluate the effect of graphene-coating on the electrode resistance. The EIS spectra were acquired after the 1st charge (Figure 3B) and the 20th charge (Figure 3C) from the bare and the graphene-coated samples. The EIS spectra from charged LiCoO₂ exhibits an initial intercept, two semicircles and a 45° inclined line at various frequency regions. The first intercept of the Nyquist plot, R_s represents the internal resistance related to the electrolyte resistance and cell connections. The first semi-circle (high frequency) represents the resistance from the surface film (R_{sf}). This surface film can be either the solid electrolyte interface (SEI) or the rGO coating or a combination of both. Formation of a SEI on the surface of bare-LiCoO₂ as a surface film during the first charge has been well-documented in the literature.^[83,85,86] Prior reports

have shown that the SEI is predominantly composed of Li₂CO₃ and LiOR,^[86] where R-groups correspond to the organic species from the electrolyte. Although this surface film is known to protect the electrode from further side reactions, it is not stable and can decompose rapidly at high voltage or high temperature.^[85] The decomposition and reformation of such surface film can result in electrolyte consumption, cathode surface phase transition and increase in the resistance.^[83,86] The second semicircle at middle frequency describes the lithium-intercalation process, which is also known as charge transfer at electrode/electrolyte interface (R_{CT}). Here the very low frequency regime is attributed to the diffusion-controlled behavior and is shown as an inclined line with ca. 45° angle (Warburg phase).^[82] Since Nyquist plot is considering R_{real} and R_{imaginary} for X- and Y-axes, respectively, it does not have enough resolution to resolve the two different time constants at some frequency levels. This is the main reason that in both graphene coated LiCoO₂ and bare LiCoO₂ samples, R_{sf} gets coupled to R_{CT} and forms a larger semicircle. However, we can distinguish the different resistive behaviors upon running the Zsim for modeling the electrical circuit of the batteries. Zsim takes into account the precise frequencies assigned for each specific resistance and models the equivalent circuit.^[82]

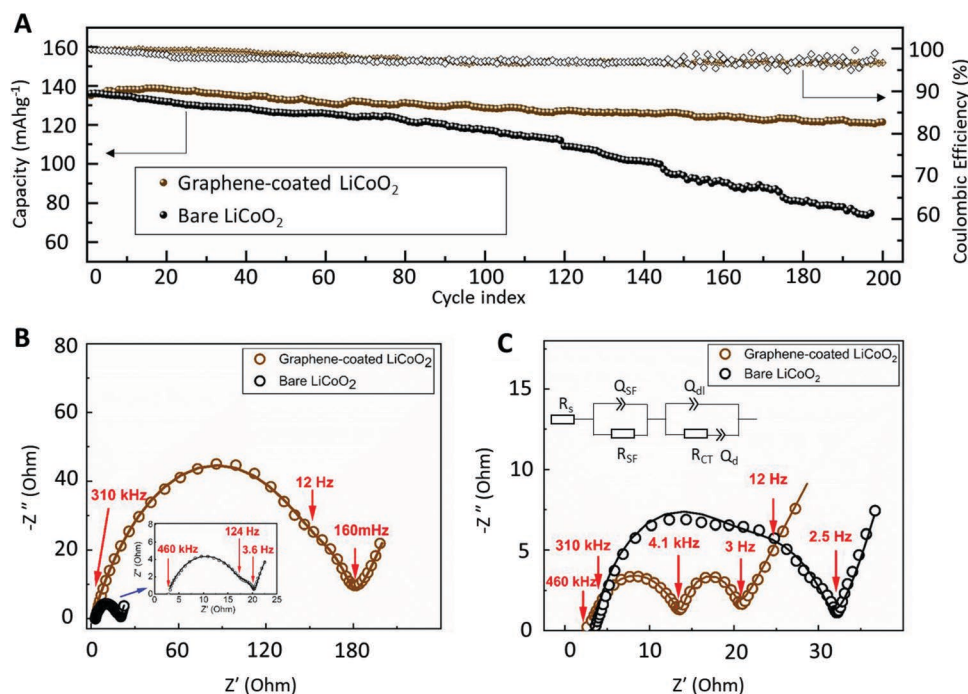


Figure 3. Electrochemical cycling and impedance spectroscopy results. A) Half-cell cycling test performed on the bare and the graphene-coated LiCoO_2 . B) Electrochemical impedance spectra from bare and graphene-coated samples after first full charge, and C) electrochemical impedance spectra after 20 cycles and full charge. The equivalent circuit is shown in inset (C).

The equivalent electrical circuit model for all EIS spectra is shown as inset in the Figure 3C. Table S1 (Supporting Information) summarizes the resistance values for the components of each spectrum based on the fitted model. The EIS spectra obtained after first charge demonstrates a large resistance in the graphene-coated LiCoO_2 . This behavior is correlated to two reasons: 1) limited Li-ion pathways in the out of plane direction of pristine rGO coating layer^[87] and 2) improved electronic conductivity of rGO coating due to electrochemical reduction during repeated cycling.^[88,89] After 20 cycles and full charge to 4.2 V, the EIS spectra from the graphene-coated sample show a remarkable decrease in both R_{SF} and R_{CT} . Specifically, R_{SF} and R_{CT} have reduced from 231.6 and 64.1 Ω at first charge to 15.3 and 9.5 Ω after 20th charge. The reduction of the surface film resistance can be attributed to the cumulative reduction of rGO during electrochemical cycling,^[90–92] which results in improved conductivity of the solid electrolyte interface after initial cycles. In addition, the reduction of R_{CT} can be attributed to the formation of Li-ion transfer pathways in the rGO layers during the initial cycles, where repeated Li transfer causes defect formation and further lowers the measured resistance.^[87] In contrast, the EIS results from the bare LiCoO_2 after the 1st and the 20th charge show that there is an increase both in R_{SF} (from 17.3 to 21.1 Ω) and R_{CT} (from 6.1 to 14.0 Ω) during cycling. The increase in R_{SF} can be explained by the instability and degradation of the surface film due to the cathode surface degradation and Co dissolution, and increase in R_{CT} can be attributed to the surface phase transitions. Overall, based on the EIS results it can be concluded that the graphene-coating process does not increase the cell resistance and alleviates the surface degradation of cathode particles by

providing a protective coating on the cathode particles surface, thus decreasing the charge transfer and solid/surface film resistance. To further evaluate the technological implication of this research, structural and morphological studies of rGO-coated cathode subsequent to prolonged electrochemical cycling should be carried out in future.

To test the structural stability of the samples under thermal abusive conditions, we performed in situ heating TEM experiments on the bare and the graphene-coated Li_xCoO_2 samples. It is known that the pristine LiCoO_2 is thermally stable and oxygen release occurs after delithiation due to the formation of under-coordinated oxygen atoms.^[31] Therefore, the bare and the graphene-coated samples were cycled three times and charged to 4.2 V to obtain $\text{Li}_{0.5}\text{CoO}_2$.^[93] Figure 4A demonstrates SEM images from the graphene-coated $\text{Li}_{0.5}\text{CoO}_2$ particles after electrochemical cycling, and evidently, the rGO layer is well maintained on the surface of the particles. Charged cathode particles were extracted and loaded into the Gatan heating holder to perform the in situ heating STEM/EELS experiments. In these experiments, samples were heated to 300 $^\circ\text{C}$ incrementally at 50 $^\circ\text{C}$ steps. Based on our previous report,^[31] $\text{Li}_{0.5}\text{CoO}_2$ is thermally unstable and starts to release oxygen when heated to above 100 $^\circ\text{C}$. This oxygen release, which results in the reduction of cobalt, can be quantified by analyzing the Co L edges in the EELS signal. To quantify the Co valence state based on the EELS results, we have performed EELS calibration experiments which are explained in our previous work.^[31] Specifically, by measuring the cobalt L3, L2 edges ΔE value as a function of temperature and acquisition position, we can quantify the cobalt valence state at each point in our samples and effectively compare the bare and the graphene-coated Li_xCoO_2 structural

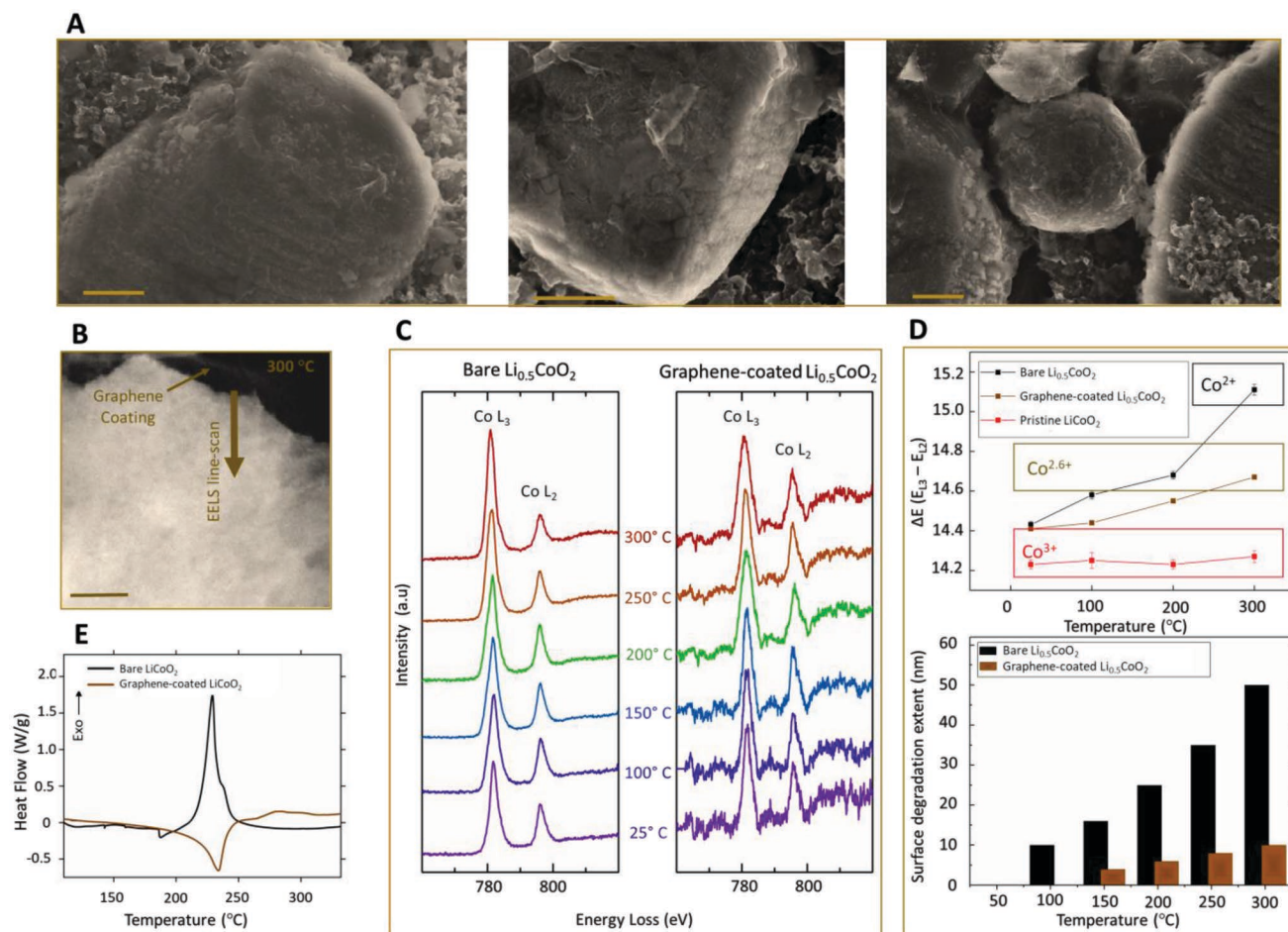


Figure 4. Thermal stability evaluation of graphene-coated $\text{Li}_{0.5}\text{CoO}_2$ sample. A) SEM images from delithiated (charged) $\text{Li}_{0.5}\text{CoO}_2$ sample (scale bars are 1 μm). B) Low magnification STEM image at 300 $^{\circ}\text{C}$ showing the presence of graphene coating (scale bar is 100 nm). C) EELS analysis results from in situ heating experiments. Reduction of cobalt at high temperatures is delayed by the presence of graphene coating. D) EELS line scan analysis results demonstrate the thickness of the layer with reduced cobalt species and released oxygen. At 100 $^{\circ}\text{C}$, no valence change could be observed at the surface of the sample. At 200 $^{\circ}\text{C}$, the thickness of the degraded layer is measured to be less than 10 nm compared to the bare sample. E) DSC results from the bare and graphene-coated $\text{Li}_{0.5}\text{CoO}_2$.

stability at high temperatures. Figure 4B shows an HAADF image from the surface of the graphene-coated $\text{Li}_{0.5}\text{CoO}_2$ particle, where a thin layer of graphene can be observed. It should be noted that, oxygen release and reduction of cobalt start from the surface areas of Li_xCoO_2 .^[31] Hence, by performing TEM experiments on the Li_xCoO_2 particles, the oxygen release is initially detected at the surface which by increasing the temperature propagates toward the core areas. Therefore, to understand the role of the graphene-coating on the oxygen release, we performed the in situ heating EELS experiments as a function of temperature and beam position. Figure 4C illustrates the EELS results obtained from the outmost ≈ 5 nm of the surface of particles. As can be seen from the analyzed results based on cobalt L3, L2 edges ΔE value in Figure 4D, Co valence change at the surface of the particle is effectively delayed by the presence of graphene layer. The reduction of Co from 3+ to 2.6+ that occurs at ≈ 100 $^{\circ}\text{C}$ in bare $\text{Li}_{0.5}\text{CoO}_2$, is postponed to higher than 200 $^{\circ}\text{C}$ for the graphene-coated sample. Also, further reduction of Co species to 2+ which is observed between 200–300 $^{\circ}\text{C}$ does not occur in the graphene-coated sample up

to 300 $^{\circ}\text{C}$. It should be noted that lower signal to noise ratio in the spectra from the graphene-coated samples is due to shorter acquisition time to avoid electron beam damage to the graphene layer. Furthermore, we performed EELS line scanning at each temperature to track the extent of oxygen release from the cathode particles. To compare the degradation extent in both samples, we considered the valence of 2.6+ as the degradation threshold and measured the degradation extent accordingly as a function of length in the bare and graphene-coated samples at each temperature. Accordingly, by reaching to 100 $^{\circ}\text{C}$, reduction of cobalt and oxygen release occurs in a layer of 10 nm at the surface of the bare $\text{Li}_{0.5}\text{CoO}_2$ particles. However, the graphene-coated sample shows higher thermal stability, and the reduction of cobalt can be seen in < 5 nm from the surface of the sample after increasing the temperature to higher than 150 $^{\circ}\text{C}$. When the temperature reaches 300 $^{\circ}\text{C}$, the thickness of this damaged layer reaches to 50 nm in the bare $\text{Li}_{0.5}\text{CoO}_2$, while it is only about 10 nm for the graphene-coated sample. These observations can be explained in two ways: 1) graphene-coating does not allow the formation and release of O_2 molecules since

oxygen species bond with carbon atoms from the rGO layer, and breaking such bonds has a high barrier energy. 2) If O_2 is formed, graphene layer inhibits the release of O_2 , which results in a O_2 rich atmosphere underneath the rGO layer that hinders the further O_2 release from the surface of the cathodes. This hypothesis is supported by the recent work from Karki et al.,^[94] where inhibiting the O_2 release from the layered oxide cathodes was achieved in O_2 -rich atmosphere. Their environmental controlled in situ heating STEM/EELS results suggest that in O_2 atmosphere oxygen release and reduction of transition metals in the layered oxide cathode framework is significantly delayed and thus the structure is more stabilized. Although, applying O_2 gas to a Li-ion battery for mitigating the thermal runaway is not a sensible approach, their study supports our hypothesis and confirms the discussed mechanism.

In addition, the oxygen release and thermal decomposition is accompanied by structural degradation and phase transformations from original layered structure to spinel and rocksalt

phases. Through dark field TEM imaging and atomic resolution STEM analysis, it has been identified that such phase transformations result in evolution of distinct spinel/rocksalt grains on the subsurface and shell of the layered cathode particles respectively.^[31] Therefore, visualization of the effect of graphene-coating on the structural stability of the $Li_{0.5}CoO_2$ particles is also possible. Movie S1 (Supporting Information), taken in the ronchigram mode from a graphene-coated $Li_{0.5}CoO_2$, illustrates the effect of graphene-coating on the structural stability of the cathode. In the Ronchigram mode, Kikuchi patterns that are the indication of crystal structure and its zone axis with respect to the electron beam will also show up. Here we demonstrate an interesting case, which is a particle with a discontinuity in the graphene coating. Due to the discontinuity in the coating layer of the shown individual particle, the effect of graphene-coating on the structural stability can be comprehended from this movie. Snapshots of this movie are shown in **Figure 5**. In the area with the presence of the graphene coating strong contrast

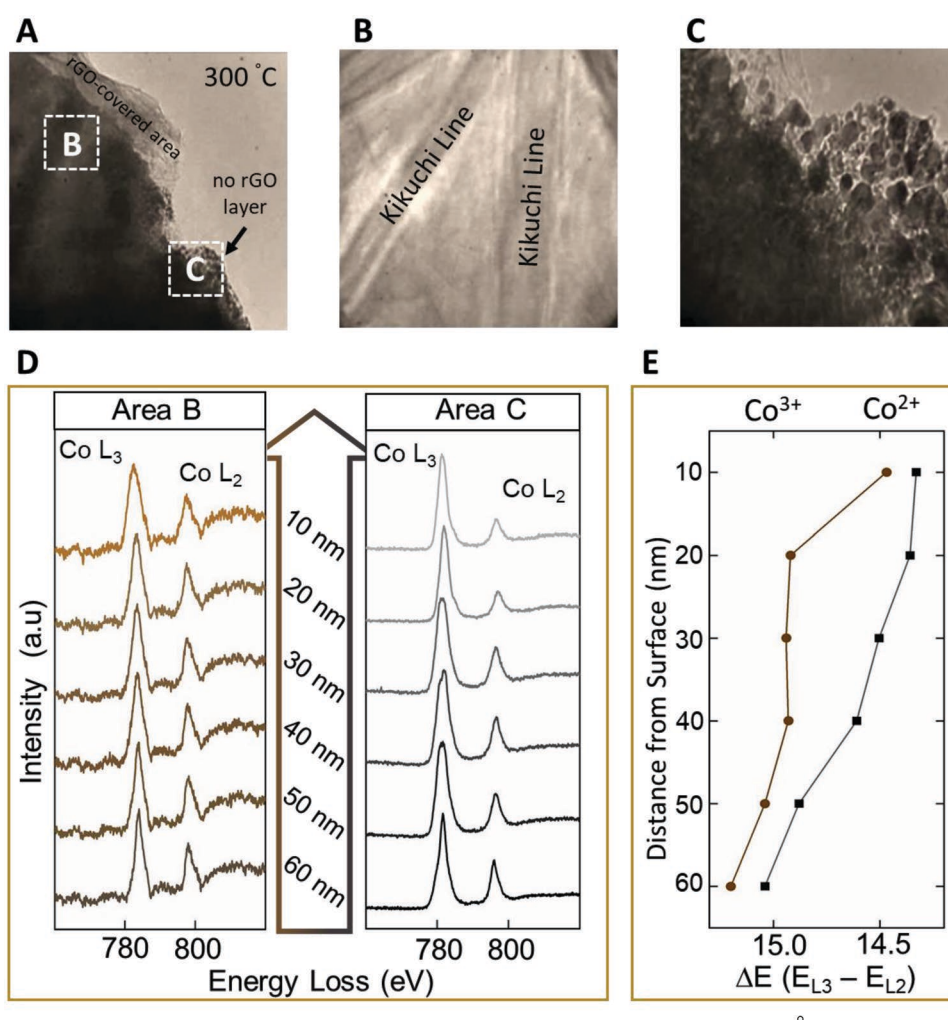


Figure 5. Snapshot from TEM movie of a partially coated $Li_{0.5}CoO_2$ at 300 °C with corresponding EELS results. A) Snapshot from the lower magnification showing an area with partial graphene coating. B) Snapshot from the graphene-covered area shows the Kikuchi pattern confirming the preserved layered structure in this area. C) Snapshot of the area without graphene-coverage shows the typical $Li_{0.5}CoO_2$ structural degradation at elevated temperatures. D) EELS line scan results obtained at 300 °C from the areas indicated in the panel (A). E) Energy difference of $Co L_3$ and L_2 edges (ΔE) as a function of distance from the surface.

from the Kikuchi pattern confirms that the layered crystal structure is maintained at 300 °C (Figure 5B). However, by looking at the area where graphene layers have been discontinued, this pattern cannot be observed which implies that the original layered structure is collapsed and disordered-spinel and rocksalt phases in small distinct grains are formed on the bare side of $\text{Li}_{0.5}\text{CoO}_2$ particle surface (Figure 5C). The evidence of phase transformation from layered structure to spinel and rocksalt phases can be found here.^[31] It should be noted that acquisition of diffraction patterns that requires high dose exposure of the electron beam on the sample and the graphene layer, can generate knock-on damage in the graphene layer and diminishes its effectiveness in suppressing the O_2 release. Therefore, ronchigram movie is presented to illustrate the effect of graphene-coating on the structural stability of the $\text{Li}_{0.5}\text{CoO}_2$ cathode. To further investigate the significance of oxygen evolution in the partially coated LiCoO_2 particles, we performed EELS line scans on areas indicated in Figure 5A at 300 °C. The line scans are obtained perpendicular to the surface of the sample on the top 60 nm distance from the surface with 10 nm step size (Figure 5D). Results are analyzed based on the energy difference between Co L_3 and L_2 edges. By plotting the results from each point as a function of ΔE , it can be observed that Co species in areas with graphene-coverage are reduced from 3+ to 2+ only in the top 10 nm layer and the Co species in underneath areas maintain their valence state (Figure 5E). In contrast, the reduction of Co species in the noncoated areas grew for 50 nm underneath of the surface. It should be noted that these numbers represent the lateral distance of the analyzed points from the surface of the specific particle and do not correspond to the thickness or the cross section of particles. To deconvolute the effect of bulk from the surface and to compare the oxygen release and metal reduction only at the surface of cathode particles, in situ heating XPS experiments are suggested to be carried out in future studies.

In addition, bulk scale characterization of the thermal stability of the cathode sample has been carried out by DSC experiments. Figure 4E corresponds to the DSC results from the bare and graphene-coated cathode that have been charged to 4.2 V after two charge/discharge cycles. The sharp exothermic peak, which can be seen around 210 °C in the DSC curve from the bare $\text{Li}_{0.5}\text{CoO}_2$ is the result of highly exothermic reaction between the flammable gases evolving from the electrolyte and the released oxygen from the cathode. It should be noted that, the DSC results were performed in the hermetically sealed containers to keep the released flammable gases and oxygen inside to complete the reaction. Interestingly, the results from the graphene-coated $\text{Li}_{0.5}\text{CoO}_2$ shows a significant reduction in the extent of this exothermic reaction and almost no exothermic event can be recorded from this sample, which means that oxygen evolution is extensively hindered due to the graphene-coating process. The experiments were performed on more samples to ensure the reproducibility.

To explain the experimental observations and to understand how the graphene coating could prevent/delay the release of oxygen from the cathodes surface, comprehensive computational modeling, utilizing density functional theory (DFT) and ab initio molecular dynamics (AIMD) were carried out. Using such complementary modeling techniques, we studied the

effect of graphene coating on the activation/barrier energy of the O_2 release reaction as well the dynamics of the rGO/LCO surface interactions at the atomic scale. The details of the DFT model configuration are discussed in the Supporting Information. Before proceeding to compute the reaction energies and activation barriers for O_2 formation in presence of rGO coating, we carried out cNEB calculations to obtain activation energies for O_2 formation in the bare (012) and (104) facets of $\text{Li}_{0.5}\text{CoO}_2$. Here, the reaction energy is defined as the energy of the product minus the energy of the reactant. Meanwhile, the activation energy is defined as the energy difference between the ground state energy and the transition state. It is important to note that zero-point energies are not included for the calculation of these electronic energies. Based on our previous study, side facets are more prone to oxygen release compared to the top (001) facet.^[31] Therefore, side facets such as (012) and (104) that are prone to oxygen release are chosen for the modeling in this research. Optimized structures are used as the initial state structures for cNEB calculations. For final state structures, one $\text{O}_{\text{cathode}}$ atom was removed from the $\text{Co}-\text{O}_{\text{cathode}}$ bond and located near an adjacent $\text{O}_{\text{cathode}}$ atom to recombine as an O_2 molecule with an $\text{O}-\text{O}$ bond length of 1.25 Å. Our results indicate that the motion of a surface $\text{O}_{\text{cathode}}$ atom to recombine as an O_2 molecule with a nearest-neighbor O atom occurs by a jump of ≈ 2.82 Å. The reaction energies at the (012) and (104) facets are -1.61 and -1.72 eV, respectively. These energies are highly exergonic indicating that both facets are expected to undergo O_2 formation under nonequilibrium conditions. The cNEB calculations show that the O_2 formation at the bare (012) and (104) facets need to overcome the activation energies of $E_{\text{activation}} = 0.14$ and 0.23 eV, respectively (Figure 6A). The Arrhenius equation $\kappa = \nu \cdot e^{-\frac{E_{\text{activation}}}{kT}}$ with a prefactor of $\nu = 10^{13} \text{ s}^{-1}$ yields that the time to see an O_2 formation event at 400 °C at the (012) and (104) facets are very close and have an average of 3.20 ps. This evolution time is in the same order of magnitude of events observed in AIMD simulations that will be discussed later on.

Next, we calculated the O_2 formation energy barrier at the facets in the presence of a rGO coating material. As discussed in the Supporting Information, the undercoordinated $\text{O}_{\text{cathode}}$ atoms form chemical bonds with C atoms from the graphene layer. Following the procedure described in the previous section, which is inducing O_2 formation through breaking the $\text{Co}-\text{O}_{\text{cathode}}$ bonds at the rGO-coated facet, we observed that the $\text{O}_{\text{cathode}}$ atom is rejoining the C atom from rGO layer. In other words, the simulations show that no O_2 formation can be observed in presence of a fully covered rGO coating. This is because complete coordination of oxygen atoms by bonding with the C atoms from the rGO layer. As another condition, we assume that the rGO material is not covering the complete surface and there are uncovered domains in the rGO coating layer such as defect sites. We considered that the first O atoms are bonded to the C atom from the graphene layer and the second O atoms are in the defective area and are undercoordinated. Our calculation demonstrates that formation of an O_2 molecule at the (104) facet under the described circumstances yields a reaction energy of $E_{\text{reaction}} = -0.88$ eV and an activation energy barrier of $E_{\text{activation}} = 2.77$ eV. According to the Arrhenius equation, such reaction will take more than 16 600 h to

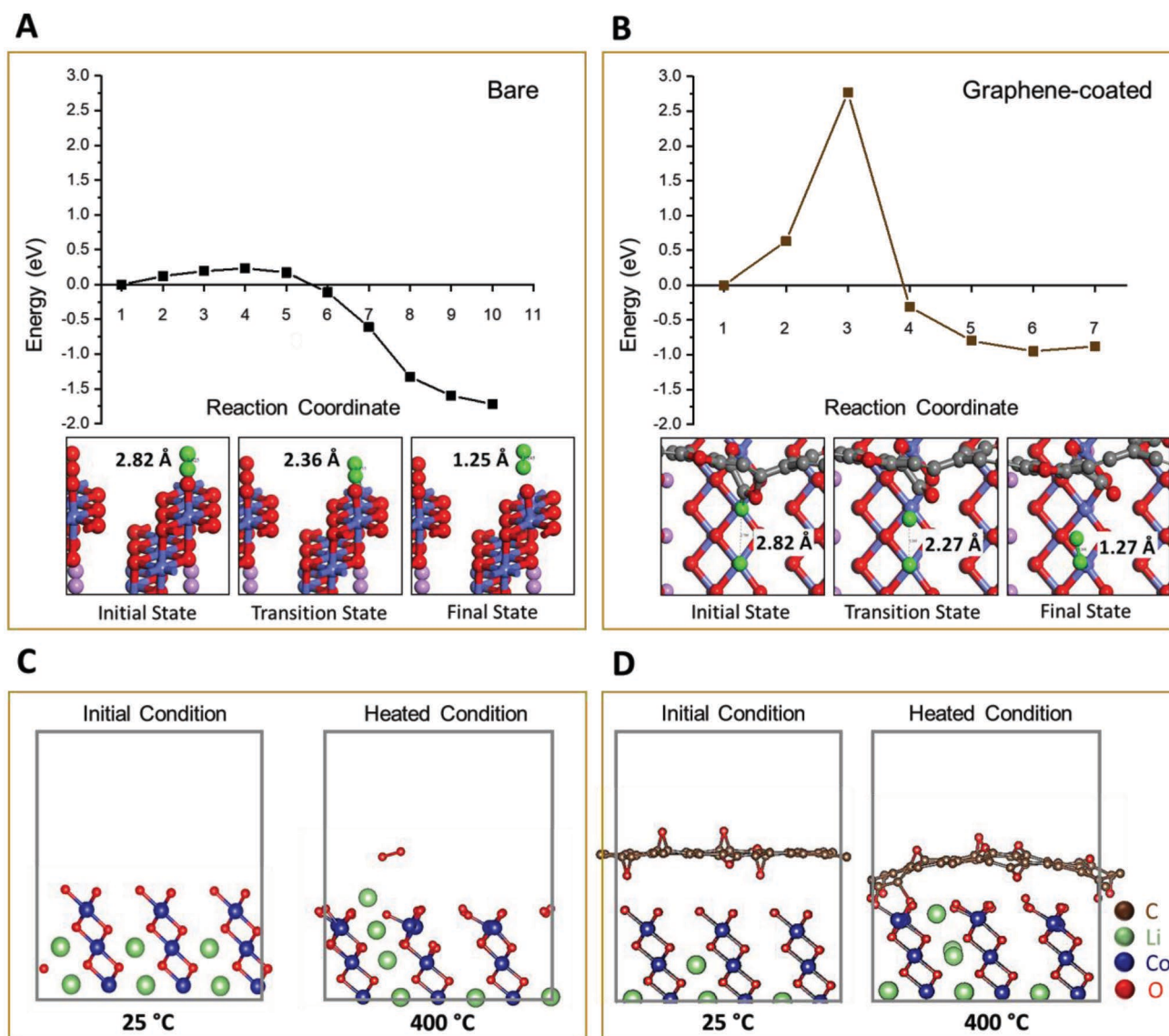


Figure 6. O₂ formation energy profile based on DFT calculations and AIMD modeling results. A) Energy profile for O₂ formation for the bare Li_{0.5}CoO₂. B) Energy profile for O₂ formation for the rGO coated Li_{0.5}CoO₂. Snapshots of the initial state (IS), transition state (TS), and final state (FS) structures are also shown. Green spheres represent O_{cathode} atoms forming the O₂ molecule. C) AIMD results from the bare Li_{0.5}CoO₂ (012) slab at 25 and 400 °C after 400 fs. D) AIMD results from the rGO coated Li_{0.5}CoO₂ (012) slab at 25 and 400 °C after 4320 fs.

happen at 400 °C, which is kinetically unfeasible. So it can be concluded that, while the bare surfaces are expected to undergo O₂ evolution within the first few picoseconds, the rGO coating material forms a stable interface with the side facets due to its chemisorption via C–O_{cathode} bond formation, leading to higher reaction energies and activation barriers of the O₂ formation at nonequilibrium conditions. Figure 6A, B demonstrate O₂ formation Energy profile based on DFT calculation for the bare and the rGO coated (104) slabs together with the snapshots of the initial state (IS), transition state (TS), and final state (FS).

Moreover, AIMD simulations were performed to better understand the interaction of the rGO-coating layer with the Li_xCoO₂ species at the elevated temperature. Figure 6C shows the AIMD results from the bare (012) facet of Li_{0.5}CoO₂ before and after temperature elevation, where rapid release of O₂

molecule can be observed after 400 fs. It should be noted that it is very well known that the DFT PBE exchange-correlation functional overestimates O₂ atomization energies,^[95] which may lead to the extremely rapid release of O₂. Hence, we applied PBE + vdW + U (U–J correction of 4.75 eV only applied to the Co atoms), and we also tested alternative approaches using the revised PBE (revPBE) + vdW + U and plain PBE methods to maximize the accuracy of our results. We checked the evolution of the bare and rGO-coated (012) Li_{0.5}CoO₂ by AIMD simulations starting from the revPBE + vdW + U (see the Supporting Information for further clarification). Results from rGO interaction with the Li_{0.5}CoO₂ side slab (Figure 6D) indicate that, at 400 °C, the rGO layer moves closer to the Li_{0.5}CoO₂ surface slab and C atoms from the rGO layer form bonds with the under-coordinated O atoms found at the surface. The C–O bond

formation takes place within the first 500 fs of the simulation time. Therefore, the formation of the C–O bonds prevents the formation of O₂ molecules. After 4 ps of the simulation time, our simulations of the rGO/Li_{0.5}CoO₂ (012) interface indicates some O₂ evolution, which is a significant delay compared to the O₂ formation in the span of 500 fs in the bare sample.^[31] This is in accordance with the experimental results that show a reduction of Co species at the surface of the graphene-coated Li_{0.5}CoO₂ with a delay and to lower extent compared to the bare sample. Overall, by studying the dynamics of the rGO/Li_xCoO₂ interfaces at 400 °C we conclude that the graphene-coating improves the structural stability of the facets by two mechanisms; 1) graphene-coating does not allow the formation and release of O₂ molecules since oxygen species bond with carbon atoms from the rGO layer. 2) If O₂ is formed in the defective sites of rGO coating, graphene layer inhibits the release of O₂, which results in a O₂ rich atmosphere underneath the rGO layer that hinders the further O₂ release from the surface of the cathodes.^[94] Noteworthy, authors acknowledge that the trajectory times in AIMD modeling are in the span of pico-seconds and may not capture all the possible reaction in a certain system. Therefore, we performed both DFT and AIMD modeling to compensate such fundamental shortcomings of each modeling approach and obtain the most reliable and accurate understanding.

3. Conclusion

In summary, this work proposes graphene-coating of LiCoO₂ to suppress the oxygen release from oxide-based cathodes. Our electrochemical cycling and in situ DEMS results show that graphene-coating impedes the degradation of LiCoO₂ under high cutoff voltage cycling. In situ TEM/EELS technique and thermal analysis show that the reduction of Co species and oxygen release is effectively suppressed with the presence of graphene layer. The mitigation of oxygen release by graphene-coating has been explained in two ways: 1) bonding between the oxygen atoms from the cathode surface with carbon atoms from the rGO coating increases the energy barrier for O₂ formation and 2) the impermeable graphene layer hinders the release of any formed O₂, thus results in a O₂ rich atmosphere underneath the rGO layer that hinders the further O₂ formation from the surface of the cathodes. Overall, we believe these results pave the roadmap for the design of thermally stable oxide cathodes enabled by two-dimensional materials. Such realization is critical for *safe*, high-voltage cathodes. Another advantage of our approach is its economic viability since our graphene-coating technique is simple, effective, and scalable for large-scale applications.

4. Experimental Section

Sample Preparation: In this study, commercially available LiCoO₂ (Sigma-Aldrich) sample was used as the baseline sample. Graphene coating was carried out using commercially available aqueous dispersed monolayer graphene-oxide (Graphenea). The method of graphene coating is described in previous publications. In brief, for achieving graphene-coating on individual particles, surface charge modification should be

carried out on LiCoO₂ sample. To do so, LiCoO₂ (1 g) was dispersed in methanol (100 mL) and sonicated. Then aminopropyltrimethoxysilane (1 mL) was added to the solution and stirred for 24 h. The sample was then vacuum filtered and washed several times with methanol to obtain the positive surface charged LiCoO₂. Graphene-coated LiCoO₂ particles then can be obtained as a result of attractive electrostatic force between positively charged LiCoO₂ and negatively charged graphene oxide nanosheets. At this step, surface charged LiCoO₂ and graphene oxide nano sheets are redispersed in methanol with the concentration of 10 mg/mL and water dispersed graphene-oxide nanosheets are added dropwise to the solution. As the self-assembly takes place, graphene-coated LiCoO₂ precipitate. Finally, hydrazine (1 mL per 100 mL of cathode solution) was added dropwise to the solution to reduce the GO layer to rGO to enhance the conductivity of the coating layer. The sample is then vacuum filtered to obtain the graphene-coated LiCoO₂ particles. Noteworthy, the cost of such process is calculated to be ≈\$0.48/gr of LiCoO₂ in laboratory scale, from which only 3.3% is for consumed GO material and the rest relates to the cost of surface charge modification and hydrazine treatment that can be reduced in industrial scale.

SEM Imaging: SEM was carried out using a Carl-Zeiss electron microscope integrated into a Raith e-LiNE plus electron-beam lithography system. The acceleration voltage was set at 10 kV, and aperture size of 30 μm was used.

Raman Spectroscopy: Raman results were obtained from a Renishaw inVia Reflex Raman system equipped with a green 532 nm/50 mW diode-pumped solid-state laser. Spectroscopy was performed using a 50x objective lens. Dwell time, and laser strength were set to 100 s and 5% to obtain the best signal to noise ratio and avoid the laser-induced damage in the samples.

XPS: X-ray photoelectron spectroscopy was carried out using a Kratos AXIS-165 XPS system, equipped with a monochromatic Al Kα source (1486.7 eV). Survey spectra were collected with a pass energy of 80 eV, step size of 1 eV and dwell time of 200 ms. High-resolution regional spectra were collected with a pass energy of 20 eV, step size of 0.1 eV and dwell time of 1000 ms.

Electrochemical Cycling: Coin-type cells composed of LiCoO₂/Li half cells, glass fiber separator and 1 M LiPF₆ in EC/DMC = 1:1 electrolyte were fabricated for electrochemical tests. LiCoO₂ laminates with the composition of 80 wt% of active material, 10 wt% of carbon black, and 10 wt% of poly(vinylidene fluoride) were mixed with N-methylpyrrolidone and casted on Al foils, then dried at 80 °C in vacuum.

DEMS: The DEMS experimental setup was consisted of an MTI potentiostat, a mass spectrometer (Hiden Analytical) and a Swagelok type cell with the air outlet on the cathode side. The cell was composed of LiCoO₂ and Graphene coated- LiCoO₂ samples coated on aluminum mesh as the cathode, 0.5 mm stainless steel spacer, 0.25 mm thick lithium chip, a 0.26 mm thick glassy fiber separator, and 1 M LiPF₆ in EC:DMC electrolyte (30 μL). To measure the evolution of oxygen during charging experiment, the cell and DEMS capillary was purged with Argon to remove any impurities before the experiment.

In Situ Heating STEM/EELS Characterization: After electrochemical cycling, the coin cells were disassembled, and the cathode laminates were submerged into dimethylcarbonate for 1 h then rinsed with fresh dimethylcarbonate and dried under vacuum overnight. The laminates then were scratched, and the obtained powder was dispersed in methanol, sonicated and drop casted onto lacy carbon grid and loaded into the microscope with minimum exposure to air. Gatan double tilt heating stage was utilized for in situ heating experiments. Samples were subjected to high temperatures ranging from 25 to 450 °C with a heating rate of 10 °C min⁻¹; before collecting data, the samples were kept at the desired temperature for 15 min to ensure holder stability and temperature uniformity. STEM/EELS investigations were performed using JEOL JEM-ARM200CF STEM equipped with a cold field emission gun with 0.78 Å spatial resolution and a Gatan EnfiNA EELS system. A 22 mrad probe convergence angle was used to perform STEM imaging. HAADF detector with 90 mrad inner-detector angle was utilized to obtain Z-contrast atomic-resolution images. Spectroscopy was done with 0.1 eV/channel dispersion and with a 2 mm detector aperture.

Full-width half maximum of zero loss peak was measured 0.6 eV which determines the energy resolution of the obtained spectra.

DSC: TA Instruments Q2000 DSC systems were utilized to perform the thermal analysis experiments. To capture the heat flow from the exothermic reaction between flammable gases (from the decomposition of electrolyte) and the evolved oxygen (from the charged LiCoO_2), the hermetically sealed aluminum containers were utilized. Bare and graphene-coated LiCoO_2 samples were cycled twice and then charged to 4.2 V. Then the cells were opened in Argonne filled atmosphere, and the cathode foils were sealed in the aluminum container without drying or removing the electrolyte. DSC experiments were performed in the range of 25–350 °C with the heating rate of 2 °C min⁻¹.

Supporting Information

Supporting Information is available from the Wiley Online Library or from the author.

Acknowledgements

This project was financially supported by National Science Foundation (Award No. CMMI 1619743). The computational data is based upon work supported by the U.S. Department of Energy's Office of Energy Efficiency and Renewable Energy (EERE), as part of the Battery 500 Consortium, Award Number DE-EE0008210. Supercomputer resources from the Texas A&M University High Performance Computer Center and Texas Advanced Computing Center (TACC) are gratefully acknowledged. The acquisition of the UIC JEOL JEM-ARM200CF was supported by an MRI-R2 grant from the National Science Foundation (Award No. DMR-0959470). The work of A.S.-K. was supported by the National Science Foundation DMREF Grant 1729420. J.L. and K.A. gratefully acknowledge support from the U. S. Department of Energy (DOE), Office of Energy Efficiency and Renewable Energy, Vehicle Technologies Office. Argonne National Laboratory is operated for DOE Office of Science by UChicago Argonne, LLC, under contract number DE-AC02-06CH11357. This work made use of instruments in the Electron Microscopy Service (Research Resources Center, UIC). S.S.A. and R.S.Y. initiated the idea and designed the experimental protocols. S.S.A. and T.F. carried out the graphene-coating and the characterization efforts. S.S.A. and Y.Y. performed the electrochemical cycling experiments. S.S.A. carried out in situ TEM/EELS experiments and subsequent data analysis. M.A. and X.B. carried out the DEMS experiments, and the results were discussed and written in collaboration with A.S.K and J.L. B.S. draw the schematic figure. All the authors contributed to the writing and discussion of the manuscript.

Conflict of Interest

The authors declare no conflict of interest.

Keywords

cathode surface design, DFT/AIMD modeling, graphene-coating, in situ TEM, LiCoO_2 oxygen release, thermal degradation

Received: February 1, 2019

Revised: March 15, 2019

Published online: April 5, 2019

[1] D. Doughty, E. P. Roth, *Interface Mag.* **2012**, 21, 37.

[2] P. G. Balakrishnan, R. Ramesh, T. Prem Kumar, *J. Power Sources* **2006**, 155, 401.

- [3] N. Williard, W. He, C. Hendricks, M. Pecht, *Energies* **2013**, 6, 4682.
- [4] Q. Wang, P. Ping, X. Zhao, G. Chu, J. Sun, C. Chen, *J. Power Sources* **2012**, 208, 210.
- [5] A. Pesaran, *Adv. Automot. Battery Conf.* **2001**, 10.
- [6] S. M. Rezvanianani, Z. Liu, Y. Chen, J. Lee, *J. Power Sources* **2014**, 256, 110.
- [7] D. H. Doughty, NREL/SR-5400-54404, **2012**.
- [8] A. W. Golubkov, D. Fuchs, J. Wagner, H. Wiltse, C. Stangl, G. Fauler, G. Voitic, A. Thaler, V. Hacker, *RSC Adv.* **2014**, 4, 3633.
- [9] D. Lisbona, T. Snee, *Process Saf. Environ. Prot.* **2011**, 89, 434.
- [10] D. P. Finegan, M. Scheel, J. B. Robinson, B. Tjaden, I. Hunt, T. J. Mason, J. Millichamp, M. Di Michiel, G. J. Offer, G. Hinds, D. J. L. Brett, P. R. Shearing, *Nat. Commun.* **2015**, 6, 23.
- [11] L. Lu, X. Han, J. Li, J. Hua, M. Ouyang, *J. Power Sources* **2013**, 226, 272.
- [12] K. Zaghbi, P. Charest, A. Guerfi, J. Shim, M. Perrier, K. Striebel, *J. Power Sources* **2004**, 134, 124.
- [13] C. K. Lin, Y. Piao, Y. Kan, J. Bareño, I. Bloom, Y. Ren, K. Amine, Z. Chen, *ACS Appl. Mater. Interfaces* **2014**, 6, 12692.
- [14] S. M. Bak, E. Hu, Y. Zhou, X. Yu, S. D. Senanayake, S. J. Cho, K. B. Kim, K. Y. Chung, X. Q. Yang, K. W. Nam, *ACS Appl. Mater. Interfaces* **2014**, 6, 22594.
- [15] E. Hu, S. M. Bak, S. D. Senanayake, X. Q. Yang, K. W. Nam, L. Zhang, M. Shao, *J. Power Sources* **2015**, 277, 193.
- [16] K.-W. Nam, S.-M. Bak, E. Hu, X. Yu, Y. Zhou, X. Wang, L. Wu, Y. Zhu, K.-Y. Chung, X.-Q. Yang, *Adv. Funct. Mater.* **2013**, 23, 1047.
- [17] S. Hwang, S. M. Kim, S. M. Bak, B. W. Cho, K. Y. Chung, J. Y. Lee, W. Chang, E. A. Stach, *ACS Appl. Mater. Interfaces* **2014**, 6, 15140.
- [18] J. Geder, H. E. Hoster, A. Jossen, J. Garche, D. Y. W. Yu, *J. Power Sources* **2014**, 257, 286.
- [19] J. R. Dahn, E. W. Fuller, M. Obrovac, U. von Sacken, *Solid State Ionics* **1994**, 69, 265.
- [20] S. K. Martha, O. Haik, E. Zinigrad, I. Enxar, T. Drezen, J. H. Miners, D. Aurbach, *J. Electrochem. Soc.* **2011**, 158, A1115.
- [21] Q. S. Wang, J. H. Sun, C. H. Chen, X. M. Zhou, *J. Therm. Anal. Calorim.* **2008**, 92, 563.
- [22] A. Veluchamy, C.-H. Doh, D.-H. Kim, J.-H. Lee, H.-M. Shin, B.-S. Jin, H.-S. Kim, S.-I. Moon, *J. Power Sources* **2009**, 189, 855.
- [23] Y. Furushima, C. Yanagisawa, T. Nakagawa, Y. Aoki, N. Muraki, *J. Power Sources* **2011**, 196, 2260.
- [24] L. Wu, K. W. Nam, X. Wang, Y. Zhou, J. C. Zheng, X. Q. Yang, Y. Zhu, *Chem. Mater.* **2011**, 23, 3953.
- [25] E. Hu, S. M. Bak, J. Liu, X. Yu, Y. Zhou, S. N. Ehrlich, X. Q. Yang, K. W. Nam, *Chem. Mater.* **2014**, 26, 1108.
- [26] S. Hwang, S. M. Kim, S. M. Bak, S. Y. Kim, B. W. Cho, K. Y. Chung, J. Y. Lee, E. A. Stach, W. Chang, *Chem. Mater.* **2015**, 27, 3927.
- [27] L. Wang, T. Maxisch, G. Ceder, *Chem. Mater.* **2007**, 19, 543.
- [28] J. Zheng, T. Liu, Z. Hu, Y. Wei, X. Song, Y. Ren, W. Wang, M. Rao, Y. Lin, Z. Chen, J. Lu, C. Wang, K. Amine, F. Pan, *J. Am. Chem. Soc.* **2016**, 138, 13326.
- [29] L. Xue, S. V. Savilov, V. V. Lunin, H. Xia, *Adv. Funct. Mater.* **2018**, 28, 1705836.
- [30] B. Xiao, X. Sun, *Adv. Energy Mater.* **2018**, 8, 1802057.
- [31] S. Sharifi-Asl, F. A. Soto, A. Nie, Y. Yuan, H. Asayesh-Ardakani, T. Foroozan, V. Yurkiv, B. Song, F. Mashayek, R. F. Klie, K. Amine, J. Lu, P. B. Balbuena, R. Shahbazian-Yassar, *Nano Lett.* **2017**, 17, 2165.
- [32] J. L. Tebbe, A. M. Holder, C. B. Musgrave, *ACS Appl. Mater. Interfaces* **2015**, 7, 24265.
- [33] S. Kalluri, M. Yoon, M. Jo, S. Park, S. Myeong, J. Kim, S. X. Dou, Z. Guo, J. Cho, *Adv. Energy Mater.* **2017**, 7, 1601507.
- [34] J. Cho, Y.-W. Kim, B. Kim, J.-G. Lee, B. Park, *Angew. Chem., Int. Ed.* **2003**, 42, 1618.

- [35] I. D. Scott, Y. S. Jung, A. S. Cavanagh, Y. Yan, A. C. Dillon, S. M. George, S. H. Lee, *Nano Lett.* **2011**, *11*, 414.
- [36] K. Du, H. Xie, G. Hu, Z. Peng, Y. Cao, F. Yu, *ACS Appl. Mater. Interfaces* **2016**, *8*, 17713.
- [37] A. Zhou, W. Wang, Q. Liu, Y. Wang, X. Yao, F. Qing, E. Li, T. Yang, L. Zhang, J. Li, *J. Power Sources* **2017**, *362*, 131.
- [38] X. Dai, A. Zhou, J. Xu, Y. Lu, L. Wang, C. Fan, J. Li, *J. Phys. Chem. C* **2016**, *120*, 422.
- [39] A. Zhou, Y. Lu, Q. Wang, J. Xu, W. Wang, X. Dai, J. Li, *J. Power Sources* **2017**, *346*, 24.
- [40] J. Qian, L. Liu, J. Yang, S. Li, X. Wang, H. L. Zhuang, Y. Lu, *Nat. Commun.* **2018**, *9*, 4918.
- [41] J. S. Park, A. U. Mane, J. W. Elam, J. R. Croy, *Chem. Mater.* **2015**, *27*, 1917.
- [42] X. D. Zhang, J. L. Shi, J. Y. Liang, Y. X. Yin, J. N. Zhang, X. Q. Yu, Y. G. Guo, *Adv. Mater.* **2018**, *30*, 1.
- [43] Y. Cho, S. Lee, Y. Lee, T. Hong, J. Cho, *Adv. Energy Mater.* **2011**, *1*, 821.
- [44] B. Qiu, M. Zhang, L. Wu, J. Wang, Y. Xia, D. Qian, H. Liu, S. Hy, Y. Chen, K. An, Y. Zhu, Z. Liu, Y. S. Meng, *Nat. Commun.* **2016**, *7*, 12108.
- [45] Y. K. Sun, Z. Chen, H. J. Noh, D. J. Lee, H. G. Jung, Y. Ren, S. Wang, C. S. Yoon, S. T. Myung, K. Amine, *Nat. Mater.* **2012**, *11*, 942.
- [46] Y. Lu, A. N. Mansour, N. Yabuuchi, Y. Shao-horn, *Chem. Mater.* **2009**, *21*, 4408.
- [47] Z. Chen, Y. Qin, K. Amine, *J. Mater. Chem.* **2010**, *20*, 7606.
- [48] S. Gemini-Piperni, C. Wang, K. He, J. M. Granjeiro, S. Shafien, R. F. Klie, X. Hu, A. R. Ribeiro, T. Shokuhfar, L. A. Rocha, A. Mukherjee, R. Ghodsi, R. Borojevic, R. Shahbazian-Yassar, *Nanoscale* **2017**, *9*, 10684.
- [49] S. M. Ghodsi, C. M. Megaridis, R. Shahbazian-Yassar, T. Shokuhfar, *Small Methods* **2019**, 1900026.
- [50] N. T. Kirkland, T. Schiller, N. Medhekar, N. Biribilis, *Corros. Sci.* **2012**, *56*, 1.
- [51] S. Chen, L. Brown, M. Levendorf, W. Cai, S. Y. Ju, J. Edgeworth, X. Li, C. W. Magnuson, A. Velamakanni, R. D. Piner, J. Kang, J. Park, R. S. Ruoff, *ACS Nano* **2011**, *5*, 1321.
- [52] M. Lanza, Y. Wang, H. Sun, Y. Tong, H. Duan, *Acta Mech.* **2014**, *225*, 1061.
- [53] J. Hu, Y. Ji, Y. Shi, *Ann. Mater. Sci. Eng.* **2014**, *1*, 1.
- [54] D. Prasai, J. C. Tuberquia, R. R. Harl, G. K. Jennings, K. I. Bolotin, *ACS Nano* **2012**, *6*, 1102.
- [55] J. S. Bunch, S. S. Verbridge, J. S. Alden, A. M. Van Der, J. M. Parpia, H. G. Craighead, P. L. Mceuen, J. S. Bunch, S. S. Verbridge, J. S. Alden, A. M. Van Der Zande, J. M. Parpia, H. G. Craighead, P. L. Mceuen, *Nano Lett.* **2008**, *8*, 2458.
- [56] Y. Cui, S. I. Kundalwal, S. Kumar, *Carbon* **2016**, *98*, 313.
- [57] R. R. Nair, H. A. Wu, P. A. Jayaram, I. V. Grigorieva, A. K. Geim, *Science* **2012**, *335*, 442.
- [58] F. Guo, G. Silverberg, S. Bowers, S. P. Kim, D. Datta, V. Shenoy, R. H. Hurt, *Environ. Sci. Technol.* **2012**, *46*, 7717.
- [59] N. Yan, F. Capezzuto, G. G. Buonocore, M. Lavorgna, H. Xia, L. Ambrosio, *ACS Appl. Mater. Interfaces* **2015**, *7*, 22678.
- [60] J. Zhu, J. Lim, C. H. Lee, H. I. Joh, H. C. Kim, B. Park, N. H. You, S. Lee, *J. Appl. Polym. Sci.* **2014**, *131*, 1.
- [61] S. Pei, H. M. Cheng, *Carbon* **2012**, *50*, 3210.
- [62] Y. Zhu, S. Murali, W. Cai, X. Li, J. W. Suk, J. R. Potts, R. S. Ruoff, *Adv. Mater.* **2010**, *22*, 3906.
- [63] C. Gómez-Navarro, R. T. Weitz, A. M. Bittner, M. Scolari, A. Mews, M. Burghard, K. Kern, *Nano Lett.* **2007**, *7*, 3499.
- [64] G. Eda, G. Fanchini, M. Chhowalla, *Nat. Nanotechnol.* **2008**, *3*, 270.
- [65] S. Yang, X. Feng, S. Ivanovici, K. Mullen, *Angew. Chem., Int. Ed.* **2010**, *49*, 8408.
- [66] S. Park, J. An, J. R. Potts, A. Velamakanni, S. Murali, R. S. Ruoff, *Carbon* **2011**, *49*, 3019.
- [67] J. M. Chem, A. Liscio, P. Veronese, E. Treossi, F. Suriano, F. Rossella, V. Bellani, R. Rizzoli, P. Samori, *J. Mater. Chem.* **2011**, *21*, 2924.
- [68] Y. Wen, K. He, Y. Zhu, F. Han, Y. Xu, I. Matsuda, Y. Ishii, J. Cumings, C. Wang, *Nat. Commun.* **2014**, *5*, 1.
- [69] J. Fu, Y. Bai, C. Liu, H. Yu, Y. Mo, *Mater. Chem. Phys.* **2009**, *115*, 105.
- [70] A. Yano, M. Shikano, A. Ueda, H. Sakaebe, *J. Electrochem. Soc.* **2017**, *164*, A6116.
- [71] A. Van Der Ven, M. K. Aydinol, G. Ceder, *J. Electrochem. Soc.* **1998**, *145*, 2149.
- [72] H. Xia, Y. S. Meng, L. Lu, G. Ceder, *Adv. Mater. Mic. Nano-Sys.* **2007**, <http://hdl.handle.net/1721.1/35827>.
- [73] H. Gabrisch, R. Yazami, B. Fultz, *J. Electrochem. Soc.* **2004**, *151*, A891.
- [74] H. Wang, Y. Jang, B. Huang, D. R. Sadoway, Y. Chiang, *J. Electrochem. Soc.* **1999**, *146*, 473.
- [75] P. Yan, J. Zheng, M. Gu, J. Xiao, J. G. Zhang, C. M. Wang, *Nat. Commun.* **2017**, *8*, 1.
- [76] J. M. Tarascon, L. C. Klein, *Solid State Ionics* **1996**, *83*, 167.
- [77] J. Kikkawa, S. Terada, A. Gunji, T. Nagai, K. Kurashima, K. Kimoto, *J. Phys. Chem. C* **2015**, *119*, 15823.
- [78] H. Wang, E. Rus, T. Sakuraba, J. Kikuchi, H. D. Abruña, *Anal. Chem.* **2014**, *86*, 6197.
- [79] M. S. Whittingham, *Chem. Rev.* **2004**, *104*, 4271.
- [80] L. Hu, P. Brünner, T. Grehl, H. H. Brongersma, J. Cabana, *Chem. Mater.* **2017**, *29*, 5896.
- [81] X. Qiu, Q. Zhuang, Q. Zhang, R. Cao, *Phys. Chem. Chem. Phys.* **2012**, *14*, 2617.
- [82] Y. S. Jung, A. S. Cavanagh, A. C. Dillon, M. D. Groner, S. M. George, S. Lee, *J. Electrochem. Soc.* **2010**, *157*, A75.
- [83] K. Edstr, T. Gustafsson, J. O. Thomas, *Electrochim. Acta* **2004**, *50*, 397.
- [84] B. J. Hwang, C. Y. Chen, M. Y. Cheng, R. Santhanam, K. Ragavendran, *J. Power Sources* **2010**, *195*, 4255.
- [85] X. Dai, A. Zhou, J. Xu, Y. Lu, L. Wang, C. Fan, J. Li, *J. Phys. Chem. C* **2016**, *120*, 422.
- [86] T. Späth, D. Becker, N. Schulz, R. Hausbrand, *Adv. Mater. Interfaces* **2017**, 1700567, 1.
- [87] F. Yao, F. Gu, H. Q. Ta, S. M. Lee, S. J. Chae, K. Y. Sheem, *J. Am. Chem. Soc.* **2012**, *134*, 8646.
- [88] S. Yong, K. Shyuan, S. Kartom, W. Ramli, W. Daud, *Chem. Eng. J.* **2014**, *251*, 422.
- [89] D. P. Rocha, R. M. Dornellas, R. M. Cardoso, L. C. D. Narciso, M. N. T. Silva, E. Nossol, E. M. Richter, R. A. A. Munoz, *Sens. Actuators, B* **2018**, *254*, 701.
- [90] Z. Wang, X. Zhou, J. Zhang, F. Boey, H. Zhang, *J. Phys. Chem. C* **2009**, *113*, 14071.
- [91] G. K. Ramesha, S. Sampath, *J. Phys. Chem. C* **2009**, *113*, 7985.
- [92] Y. Shao, J. Wang, M. Engelhard, C. Wang, Y. Lin, *J. Mater. Chem.* **2010**, *20*, 743.
- [93] H. Xia, L. Lu, Y. S. Meng, G. Ceder, *J. Electrochem. Soc.* **2007**, *154*, A337.
- [94] K. Karki, Y. Huang, S. Hwang, A. D. Gamalski, M. S. Whittingham, G. Zhou, E. A. Stach, *ACS Appl. Mater. Interfaces* **2016**, *8*, 27762.
- [95] J. Paier, R. Hirschl, M. Marsman, G. Kresse, *J. Chem. Phys.* **2005**, *122*, 234102.